Supplementary Materials for

Energy Release of the 2013 M_w 8.3 Sea of Okhotsk Earthquake and Deep Slab Stress Heterogeneity

Lingling Ye, Thorne Lay,* Hiroo Kanamori, Keith D. Koper

*Corresponding author. E-mail: tlay@ucsc.edu

Published 20 September 2013, *Science* **341**, 1380 (2013)
DOI: 10.1126/science.1242032

This PDF file includes:

Other Supplementary Material for this manuscript includes the following:
available at www.sciencemag.org/content/341/6152/1380/suppl/DC1

Materials and Methods

1. Radiated Energy Estimation.

Teleseismic broadband P wave observations were analyzed for hundreds of recordings from stations of the Federation of Digital Seismic Networks (FDSN), accessed through the Incorporated Research Institutions for Seismology (IRIS) Data Management Center (DMC). High-quality signals were retained for the M_w 8.3 mainshock and M_w 6.7 aftershock for stations with computed P-wave radiation pattern coefficients higher than 0.5. Data were corrected for radiation pattern, instrument response, geometric spreading and attenuation parameterized with varying values of t^*. The low frequency portion of the average spectrum, below 0.05 Hz, is obtained from the source spectrum of the moment rate function determined by finite-fault inversion of teleseismic P waves and the long-period estimate of seismic moment, $M_0 = 4.1 \times 10^{21}$ Nm. The moment rate function characterizes the time history of the seismic radiation from the fault and is one of the most robust source attributes that can be determined using seismic waves. The higher frequency part of the source spectrum is obtained from averaging the corrected broadband P wave spectra for many stations. Subsets of 102 observations for the mainshock and 22 for the aftershock with good azimuthal distribution were used for computing individual estimates of seismic energy, and the estimates were averaged logarithmically to give the average radiated energy estimates and the average source spectra in Fig. 2.

284 pairs of recordings for the mainshock and aftershock with both signals having radiation pattern coefficients higher than 0.2 were used to compute the spectral ratio average in the passband 0.03-0.25 Hz. Examples of spectra are shown in Fig. S1. The individual spectral ratios were binned in 30° azimuthal windows and then averaged logarithmically to compute the mean value, scaled by the seismic moment of the aftershock, shown in Fig. 2.

2. Finite-fault model inversions.

We use a multi-time-window linear least-squares kinematic inversion procedure (*S1, S2*). Our initial finite-fault models (Fig. S2, S3) are parameterized with 17 nodes (central positions of subfaults) along strike and 17 nodes along dip with spacing proportional to imposed rupture velocity (3.75 km for 1 km/s, 7.5 km for 2 km/s, 11.25 km for 3 km/s, and 15 km for 4 km/s). We consider both nodal planes of the USGS W-phase point source moment tensor solution (best-double couple). The shallow-dipping plane has strike 184°, dip 10° and the steeply dipping plane has strike 12°, dip 81°. Each subfault source time function is parameterized with 4 2-s rise time symmetric triangles, allowing subfault rupture durations of up to 10 s. Rake is allowed to vary for each subevent of each subfault by allowing two rake values ±45° from the average given by the W-phase solution, with a non-negative moment constraint (*S3*). The hypocenter is 609 km deep. We apply Laplacian regularization, which constrains the second order gradient for each parameter to be zero.

75 teleseismic P wave records are used in the inversion, from global FDSN broadband seismic stations accessed through the IRIS-DMC. The data were selected from hundreds of available FDSN seismograms to have good azimuthal coverage (Figs. S9, S10) and high signal-to-noise ratios, for epicentral distances from 30° to 90°. The instrument responses are removed from the raw data to recover ground displacement records. A causal band-pass filter with corner frequencies at 0.003-0.9 Hz was applied to the data. The teleseismic Green's functions are generated with a reflectivity method that accounts for interactions in 1-D layered structures on both the source and receiver sides (*S2*). The PREM velocity structure is used in the modeling. A 60 s long time window of data with 10 s leader before the initial motion was used.

In finite-fault inversions, we usually start with a large enough fault plane to accommodate the slip zone well within it, with very low seismic moment on outer fringes of the fault model. Thus, it is necessary to trim the final slip distribution for estimating the effective rupture area. Trimming is done here by removing subfaults with a moment smaller than ξ times the moment of the subfault with the largest moment; we call ξ the trimming threshold. The purpose of trimming is twofold. First, it is to remove those subfaults with small amount of slip that can be regarded as noise in the inversion. For this purpose, a trimming threshold of ~10% is commonly used. Second, for purposes of estimating the strain energy, the stress drop to be used is $\Delta\sigma_E = \frac{\int_\Sigma \Delta\sigma_1 \Delta u_1 dS}{\int_\Sigma \Delta u_1 dS}$ which is the spatial average of stress drop weighted by slip. Unfortunately, it is difficult in practice to determine the slip distribution in sufficient detail to estimate its spatial distribution. Numerical models[18] have shown that $\Delta\sigma_E$ is always larger than the simple spatial average of the stress drop $\Delta\sigma$. Numerical calculations of $\Delta\sigma_E$ for many heterogeneous stress distributions indicate that a trimming threshold of from 0.15 to 0.3 can be used as a reasonable ratio for the purpose of estimating $\Delta\sigma_E$. We use 0.15 as the trimming parameter for all of our finite-fault models for the mainshock and aftershock. This value is slightly larger than commonly used in assessment of slip models, but it is larger not only to remove the insignificant subfaults but also to account for the effect of slip heterogeneity. Use of somewhat lower or higher trimming thresholds has negligible effects on our conclusions.

Very similar fits to global P waveforms were found for each case, despite large differences in spatial extent (Fig. S2). Slightly better fits are found using the horizontal plane, but the preference is subtle. With many-parameter space-time rupture models there is very little resolution of source finiteness for this event, as we also find to be true for the 1994 Bolivia event. Average slip values vary by a factor of 15 and static stress drop estimates by a factor of 50 for these models, so it is necessary to impose independent a priori constraints on *Vr* or fault dimensions to better constrain the source model.

The key equations for our radiation efficiency analysis are for the static stress drop for a buried rectangular fault:

$$\Delta\sigma_s = 16M_0 / (3\pi S_e W) \quad (1)$$

where S_e is the effective rupture area that gives a corresponding estimate $\Delta\sigma_E$ that we equate to the stress drop $\Delta\sigma_s$ and W is the fault width, and the radiation efficiency

$$\eta_R = E_R / \Delta W_0 = 2\mu E_R / (\Delta\sigma_s M_0) \quad (2)$$

From Fig. 4, for a given rupture velocity, we can infer a radiation efficiency value. With the measured radiated energy and seismic moment, and a rigidity appropriate for the source depth (μ = 121 x 10^3 MPa), we then know what value of stress drop will be compatible with the crack theory. For Vr = 4 km/s, η_R = 0.6 for the deep mainshock. This requires $\Delta\sigma_s$ = 15 MPa for the Mode III crack model. Given the fault length required from P wave back-projections, we can then vary the fault width, W, for finite-fault inversions to give an inverted rupture area (for a specified trimming threshold) that yields the required stress drop. This leads to W = 60 km for the Vr = 4 km/s case. The effective rupture area in that case is 9675 km^2, using a trimming parameter of 0.15. For a fixed fault width, the stress drop estimate varies inversely with the effective source area by (1), or for a fixed stress drop, the width varies inversely with the effective source area. As the stress drop increases the radiated efficiency decreases for a fixed fault width. The degree to which one wants to match the crack theory ideal constrains the precision of the stress drop estimate desired and the corresponding constraint on the rupture model spatial extent.

Final models, constrained by the results of back-projections for apparent fault length and rupture velocity and by the radiation efficiency condition, involve rectangular fault models with asymmetric bilateral grids around the hypocenter. The models with Vr = 4.0 km/s in Fig. S9 have 4 grid points along dip and 13 along strike with 15 km spacing. The along-strike spacing for Vr = 4.5 and 5.0 km/s scales proportionally (16.9 km, 18.7 km, respectively), with the number of grid points along dip being kept the same, but along strike the number of grid points reduces to 12 and 11, respectively, to bound the total fault length. Other parameters and the data set are all the same as in the initial, unconstrained models. The data are well fit by these models (Fig. S10).

3. **Back-Projection of Teleseismic P waves**

Teleseismic P waves from four geographic groupings of broadband seismometers in North America (NA) (Fig. S4a,b), Europe (EU) (Fig. S4c,d), Alaska (Fig. S5), and Australia/Southeast Asia, as well as short-period Hi-net borehole stations in Japan (JA) (Fig. S6) were back-projected to the source region (*S4*) in order to image the short-period rupture properties of the 24 May 2013 Sea of Okhotsk earthquake and its aftershocks. Seismograms were selected from each region based on uniformity of spatial sampling and similarity of the first 10 s of the unfiltered P wavetrains as defined by the average cross-correlation coefficient (*cc*) determined from a multi-channel cross correlation algorithm (*S5*). This resulted in 74 traces with *cc* > 0.7 (AK), 67 traces with *cc* > 0.5 (AU), 86 traces with *cc* > 0.7 (EU), 409 traces with *cc* > 0.75 (JA), and 164 traces with *cc* > 0.65

(NA). For AU and NA the minimum similarity threshold was decreased slightly to increase the aperture of the array, which in turn increased the slowness resolution. For JA, only traces at distances greater than 15° from the nominal epicenter were selected in order to reduce the influence of waveform complexities created by interaction with the 660-km discontinuity.

For the mainshock back-projections the U. S. Geological Survey National Earthquake Information Center hypocenter of 54.874°N 153.281°E, h=608.9 km, 05:44:49 (UTC) was used as a reference point for aligning the waveforms. The source area was gridded in increments of 0.1° in latitude from 51° to 57° and in longitude from 148° to 159° and depth was held constant at the hypocentral value. Imaging time was sampled in 1 s intervals starting 20 s before the USGS origin time and continuing for 80 s. Power was calculated from a 10-s long, tapered window that slides along beams created with fourth-root stacking. Traces were bandpass filtered between 0.5 and 2 s prior to being stacked (for the results in Fig. 3), and a 10 s long smoothing filter was applied in post-processing to reduce artifacts. The AK135 reference Earth model was used to calculate travel times. The two arrays show source durations of about 30 s, with beam power extending in a ribbon-like geometry about 40-50 km to NNE and about 120-130 km to the SSE. The dimensions are consistent with an average rupture velocity of 4 to 5 km/s, although three or four short, subevent-like bursts of energy occur during the rupture and we cannot rule out lateral and temporal variations in the rupture velocity. Animations of the time-varying sequences for the NA and EU back-projections are presented in Movie M1.

The spatial resolution of the mainshock radiation for the AK and JA arrays is poorer than that for the EU and NA arrays, however, the AK and JA arrays are aligned more closely to the mainshock rupture direction and have sensitivity to the along-strike source finiteness. We illustrate this with vespagrams of the AK (Fig. S5) and JA (Fig. S6) data. In each case the aligned traces are filtered between 0.5-2.0 s and beams are created for relative slownesses between -0.4 and 0.4 s/deg (in increments of 0.01 s/deg) using 3rd order phase-weighting stacking (*S6*), a technique that amplifies coherent energy yet causes less waveform distortion than Nth root stacking. Power is calculated in a relative, logarithmic sense from envelopes of the stacks. Both arrays show source durations of approximately 30 s, consistent with the back-projection results, but also show a shift in differential slowness as the rupture progresses. Importantly, the AK vespagram shows a drift towards negative relative slowness, indicating steeper rays and thus longer source-receiver distances, while the JA vespagram shows a drift toward positive relative slowness, indicating shallower rays and thus shorter source receiver distances as the rupture progresses. Both vespagrams are thus consistent with southward directivity of the rupture.

We confirmed the mainshock finiteness observed for the NA and EU arrays by back-projecting data from two aftershocks with very simple sources: the M_w 6.7 event that occurred at 14:56:31 (UTC) on 24 May 2013 (52.222°N, 151.515°E, depth 623.0 km), and the m_b 4.4 event that occurred at 08:58:39 (UTC) on 28 May 2013 (54.241°N, 153.395°E, depth of 627.1 km). Results are presented in Fig. S7. The NA and EU array configurations used for the three events are very similar, though not exactly the same

because of lower quality or missing data for the aftershocks. In fact, not enough high-quality data were available to perform the EU back-projection for the smaller aftershock. Nevertheless, the simplicity of the three aftershock back-projections that were successful confirm that the finiteness observed in the mainshock back-projections is related to actual source complexity and is not created by any smearing artifact inherent to back-projection or any sort of wave propagation effect.

We further examined the stability of the EU and NA results by performing five additional back-projections in a series of narrow passbands centered at 0.5 s, 1 s, 2 s, 4 s, and 8 s. The gridding was the same as described above however the time averaging was scaled according the dominant period, with beam window lengths of 1.5 s, 3 s, 6 s, 12 s, and 24 s, respectively, and post-processing smoothing filter lengths of 4 s, 6 s, 14 s, 28 s, and 50 s. Results are presented in Fig. S8 and show relatively little spatial drift compared to back-projection images for recent megathrust earthquakes, implying that the short-period and long-period energy radiated by the mainshock were not in resolvably different spatial locations for this elongate rupture.

Synthetics were computed for the model in Fig. 1 for the same stations in Europe and North America used in the back-projections, and processed in the same manner. Resulting images for back-projection of the synthetics in various passbands for rectangular models with Vr = 4.0, 4.5 and 5.0 km/s are very consistent with the observations overall (Fig. S11). In detail, the data images appear to sense the rupture front rather than the peak-slip areas, as expected for seismic radiation from a dynamic rupture. The kinematic fault models do not accurately account for high frequency radiation at the crack tip. These results are very stable compared to back-projections for shallow events because there is no interference from surface reflections. We do not include surface reflections in the imaging given uncertainty in the slab structure and strong attenuation of the depth phases.

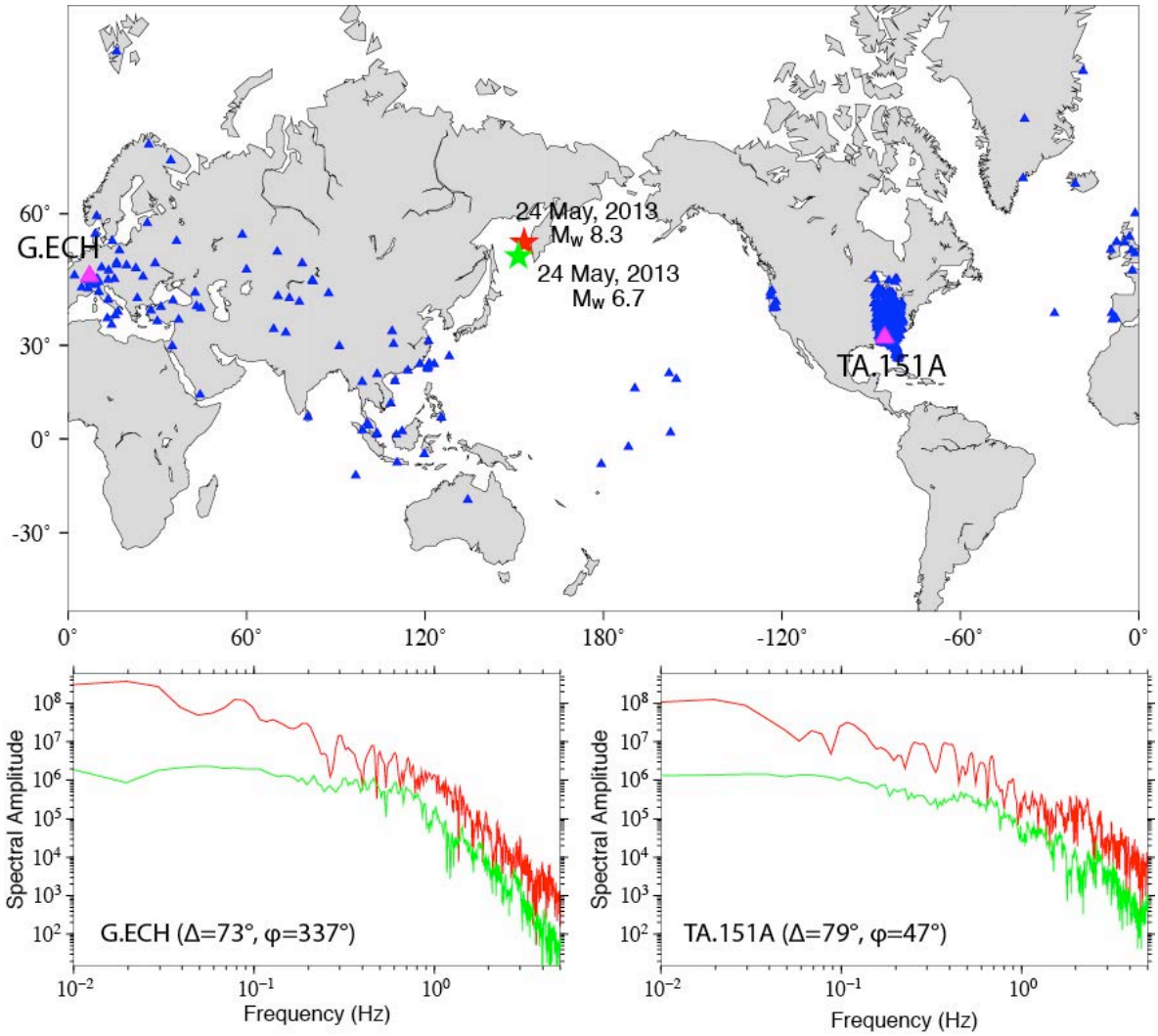

Fig. S1. Distribution of seismic stations used for spectral ratio analysis. The map shows the locations of 284 global broadband seismic network stations for which teleseismic P wave spectra were analyzed for the 24 May 2013 mainshock (M_w 8.3) (red star) and aftershock (M_w 6.7) (green star). Only stations with P wave radiation pattern coefficients larger than 0.2 for both events were used in the spectral ratio procedure. Example spectra from the stations with pink triangles on the map are shown below for the mainshock (red) and aftershock (green). Each station's epicentral distance (Δ) and azimuth (ϕ) are indicated. The spectra are corrected for relative radiation pattern and geometric spreading, but not for instrument response, which is common to the two events. The aftershock spectrum begins to drop off with frequency at around 0.5-0.6 Hz, which limits the range for which it serves as an empirical Green's function event. Spectral ratios in the passband 0.03-0.25 Hz are stacked and multiplied by the aftershock moment to obtain the mainshock source spectrum estimate in red in Fig. 2.

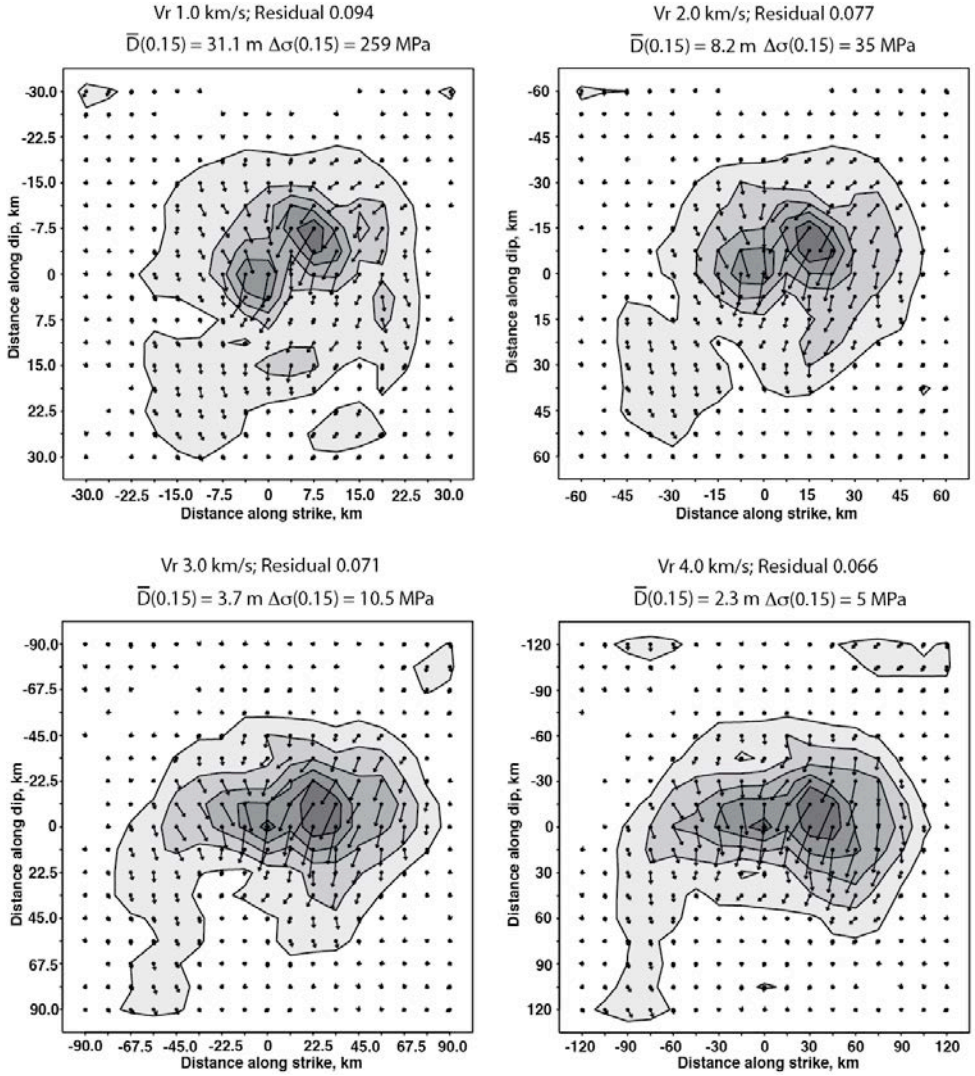

Fig. S2. Mainshock finite-fault models for varying rupture velocity for the shallow dipping plane. Slip distributions for four models with different constant rupture velocity with grid spacing scaling proportional to grid velocity. The strike is 184° and dip is 10° for all cases. Large model grids are used, with the hypocenter located at the center of each grid. For small *Vr* the rupture is relatively circular, but as it increases the model tends to elongate in the positive strike direction (toward the south). There is only about 3% greater reduction of the waveform mismatch for the much larger model for *Vr* = 4.0 km/s than for the very concentrated rupture for *Vr* = 1.0 km/s. For each model, the average displacement is computed for only those subfault sources with a seismic moment at least 15% as large as the largest sub-fault seismic moment and these values are given as D(0.15). Using the corresponding area of the remaining subfaults, a static stress drop is calculated using a circular rupture with radius matching the area of significant slip. There is about a factor of 50 range in stress drop estimate.

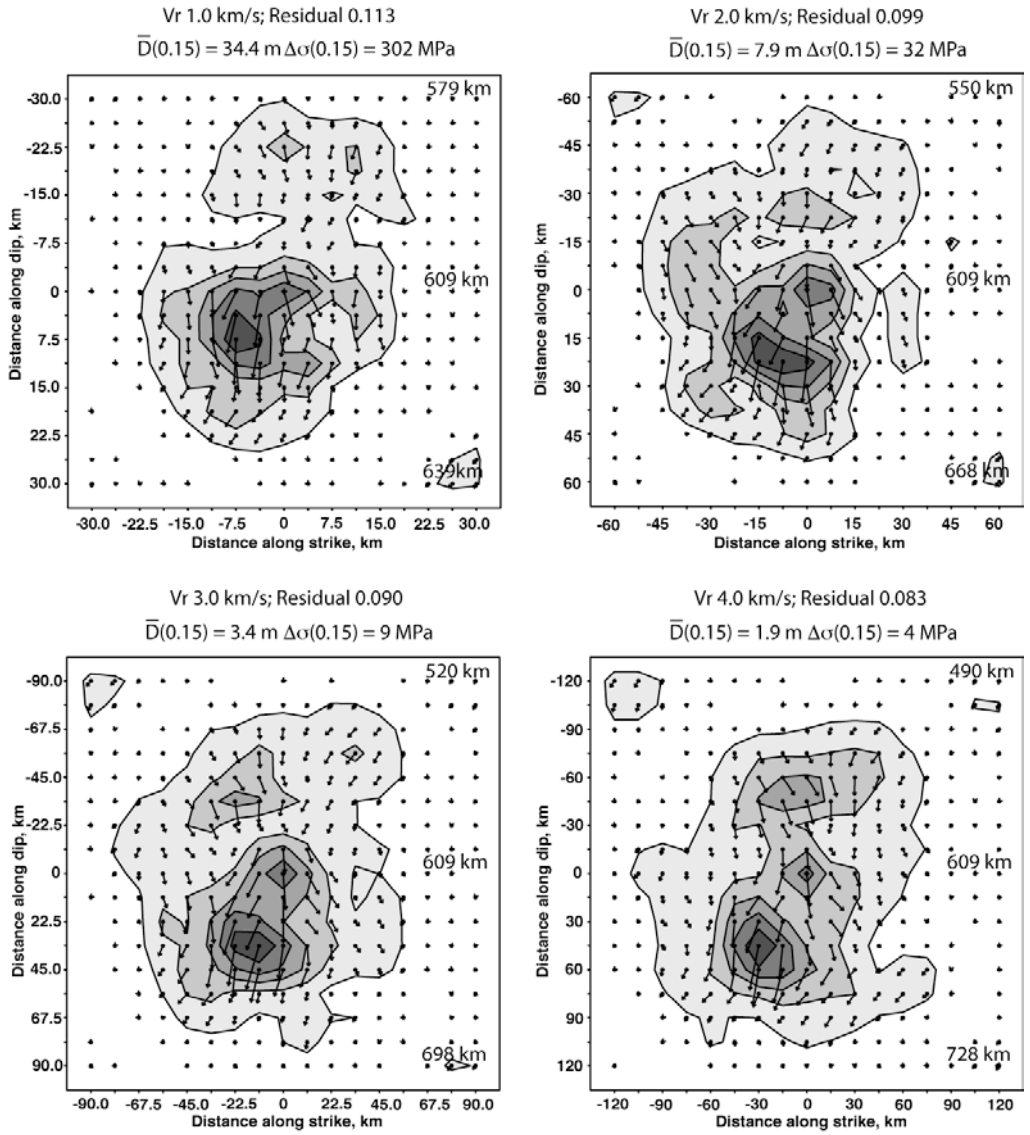

Fig. S3. Mainshock finite-fault models for varying rupture velocity for the steeply dipping plane. Slip distributions for four models with different constant rupture velocity with grid spacing scaling proportional to grid velocity. The strike is 12° and dip is 81° for all cases. Large model grids are used, with the hypocenter located at the center of each grid. For small *Vr* the rupture is relatively circular, but as it increases the model tends to elongate in the negative strike direction (toward the south). There is only about 3% greater reduction of the waveform mismatch for the much larger model for *Vr* = 4.0 km/s than for the very concentrated rupture for *Vr* = 1.0 km/s. For each model, the average displacement is computed for only those subfault sources with a seismic moment at least 15% as large as the largest sub-fault seismic moment and these values are given as D(0.15). Using the corresponding area of the remaining subfaults, a static stress drop is calculated using a circular rupture with radius matching the area of significant slip. There is about a factor of 76 range in stress drop estimate.

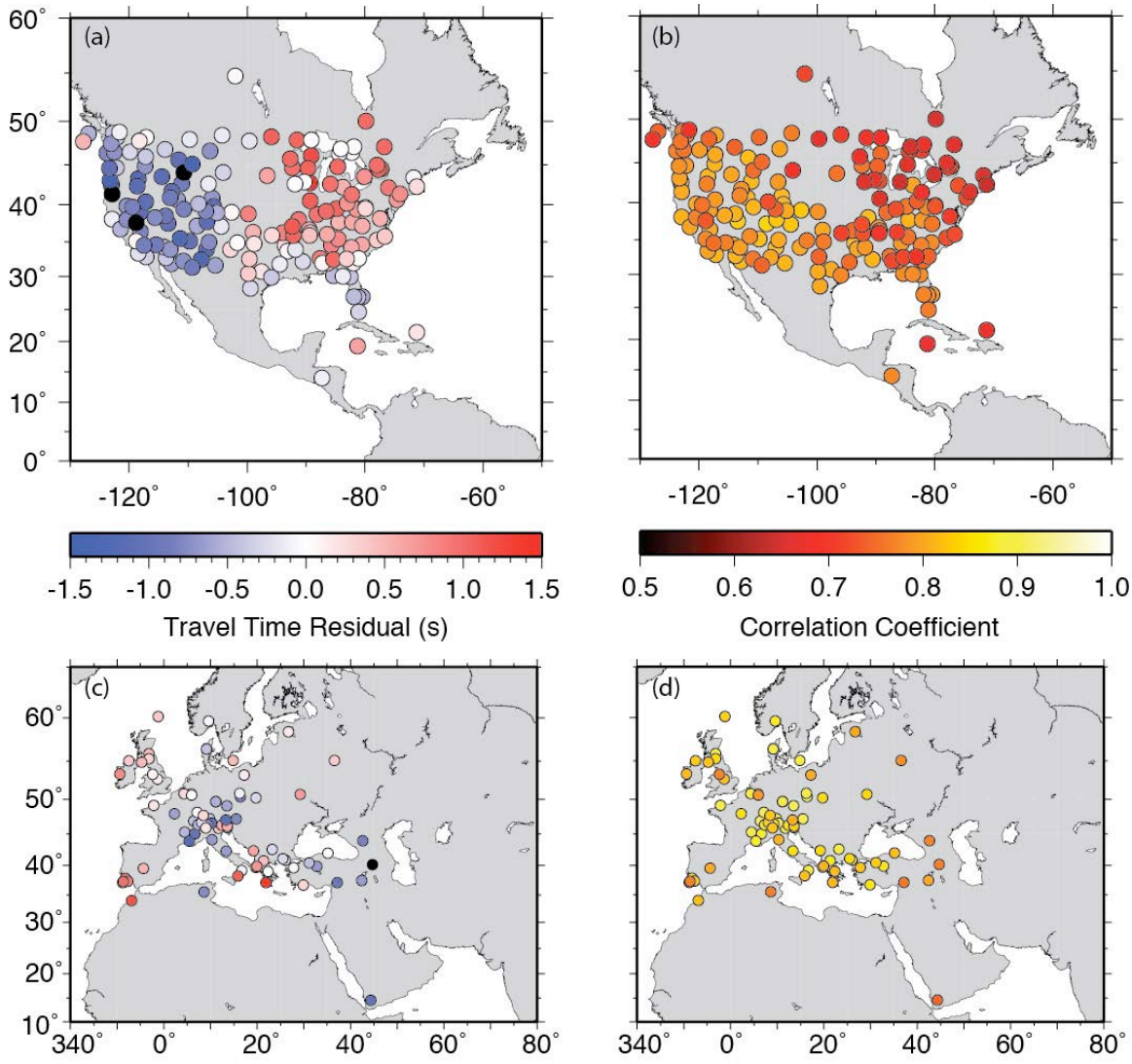

Fig. S4. Seismic station networks used for P wave back-projections. Maps of the broadband seismic station distributions in North America (a, b) and Europe (c, d) from which teleseismic P waves are obtained and back-projections to the source region performed. The station travel time residuals used to align the P waves, as determined by cross-correlation analysis are shown in (a) and (c), and the corresponding aligned trace correlation coefficients are shown in (b) and (d). The broadband traces were used for the alignment and then narrow-band filters were applied for back-projections of different passband signals. Fig. 3 shows the back-projection results for the 0.5-2.0 Hz passband data for the two networks.

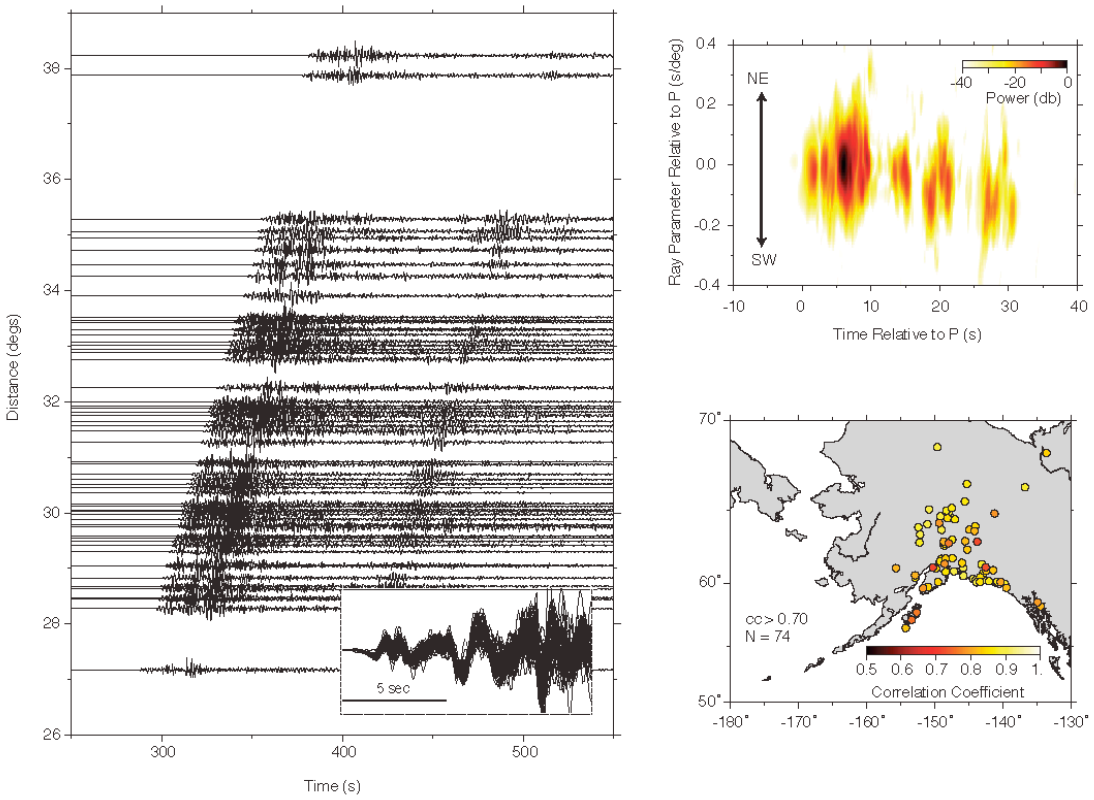

Fig. S5. Slowness variations for stations in Alaska. (a) The mainshock was well-recorded at seismic stations in Alaska, with. A profile of data is shown on the left, with the inset showing the well-correlated onset of the waveforms in the first second aligned by multi-channel correlations (the map at lower right shows the correlation coefficients for the aligned stations). The top right is a plot of travel-time ray parameter (slowness) as a function of time (vespagram). The decrease in ray parameter with time indicates that the source in rupturing away from the array (southward).

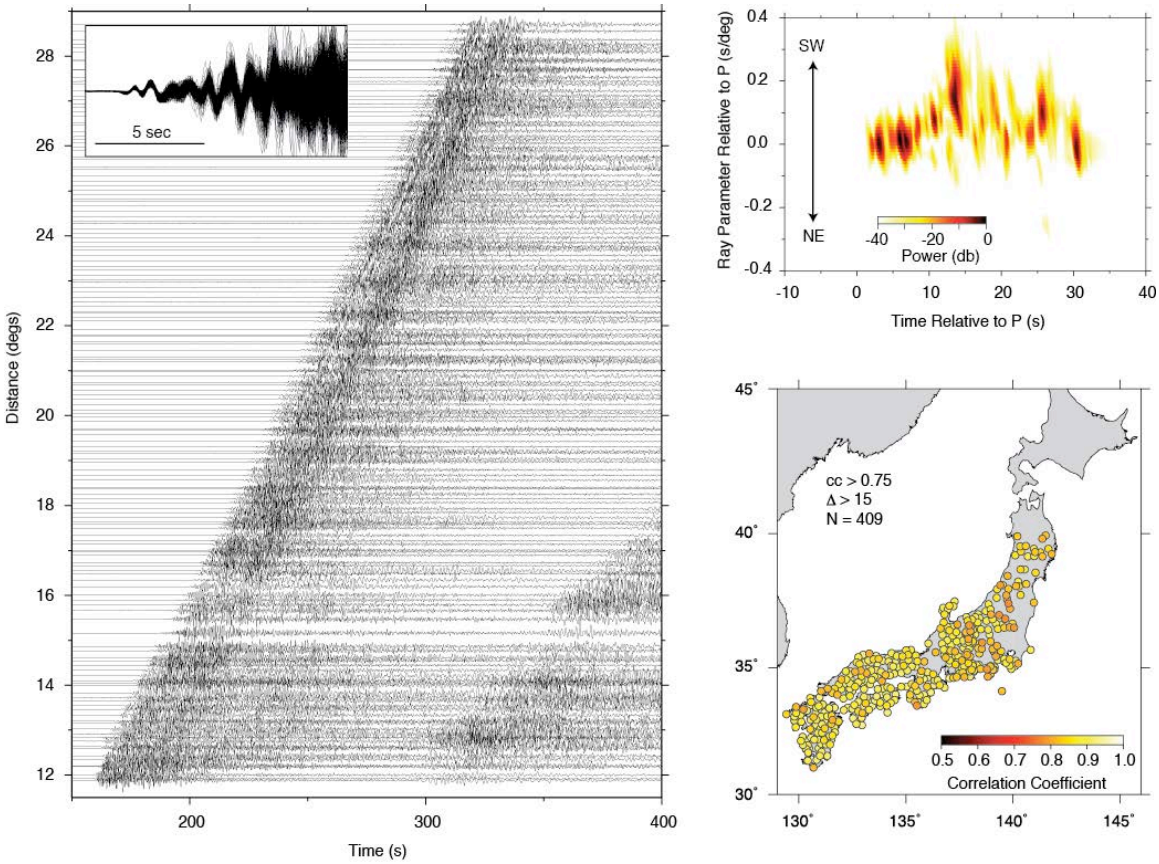

Fig. S6. Slowness variations for Hi-net stations in Japan. (a) The mainshock was well-recorded at short-period borehole stations across Japan in the Hi-net array. A profile of data is shown on the left, with the inset showing the highly correlated onset of the waveforms in the first second aligned by multi-channel correlations (the map at lower right shows the correlation coefficients for the aligned stations). The top right plot is a vespagram. The increase in ray parameter with time for the first 15 s of the waveform indicates that the source in rupturing toward the array (southward).

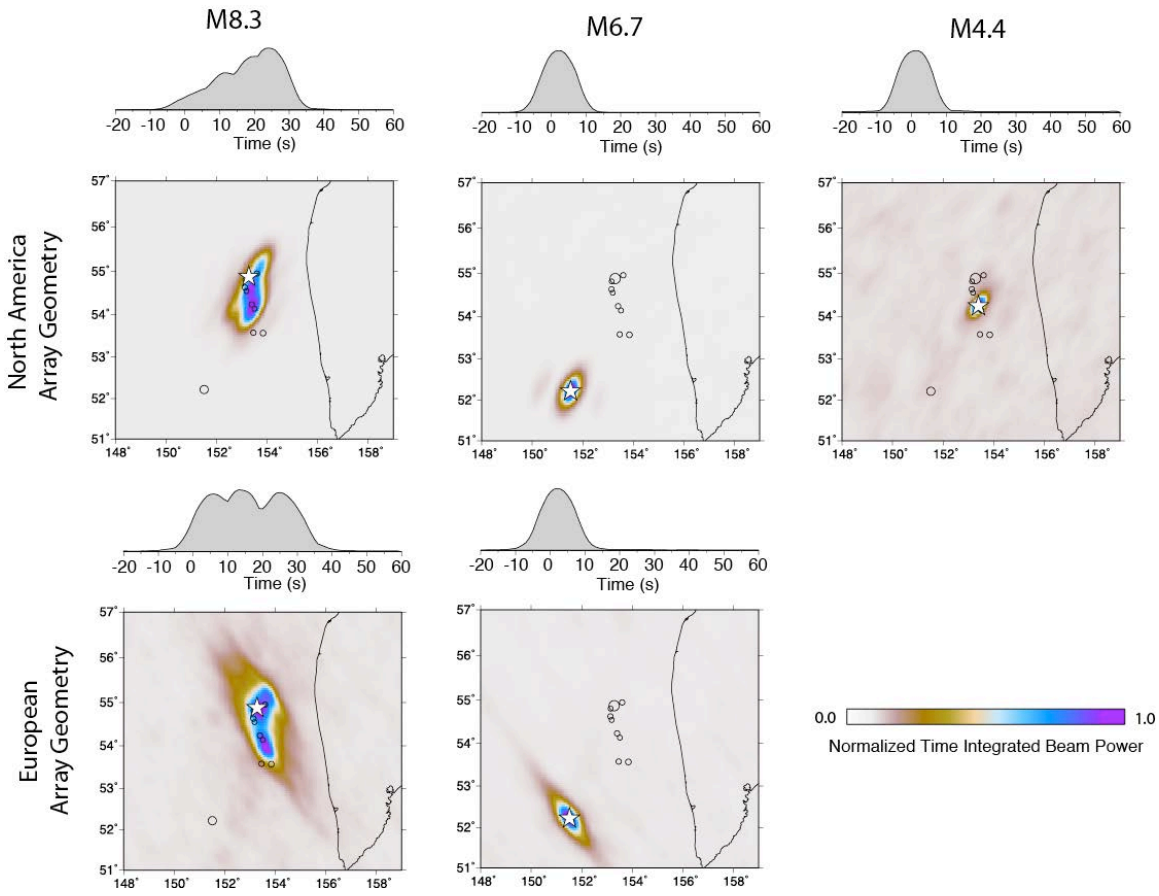

Fig. S7. Time-integrated plots of high frequency P wave back-projections for the mainshock and two aftershocks for data from North America and Europe stations. An evaluation of the network response artifacts in the back-projections for the M_w 8.3 mainshock is provided by back-projection of observations from the same stations for the M_w 6.7 aftershock and, for North America only, a m_b 4.4 aftershock. The two aftershocks should essentially be point-sources of energy due to having small spatial and temporal distributions of their energy release, and they are well imaged as spatially concentrated sources for data from both network configurations. The images with southern extension for the mainshock are thus reliable features of the finiteness, with any localized subevent pulses during the mainshock event being smeared out in the images to the same extent as for the aftershocks.

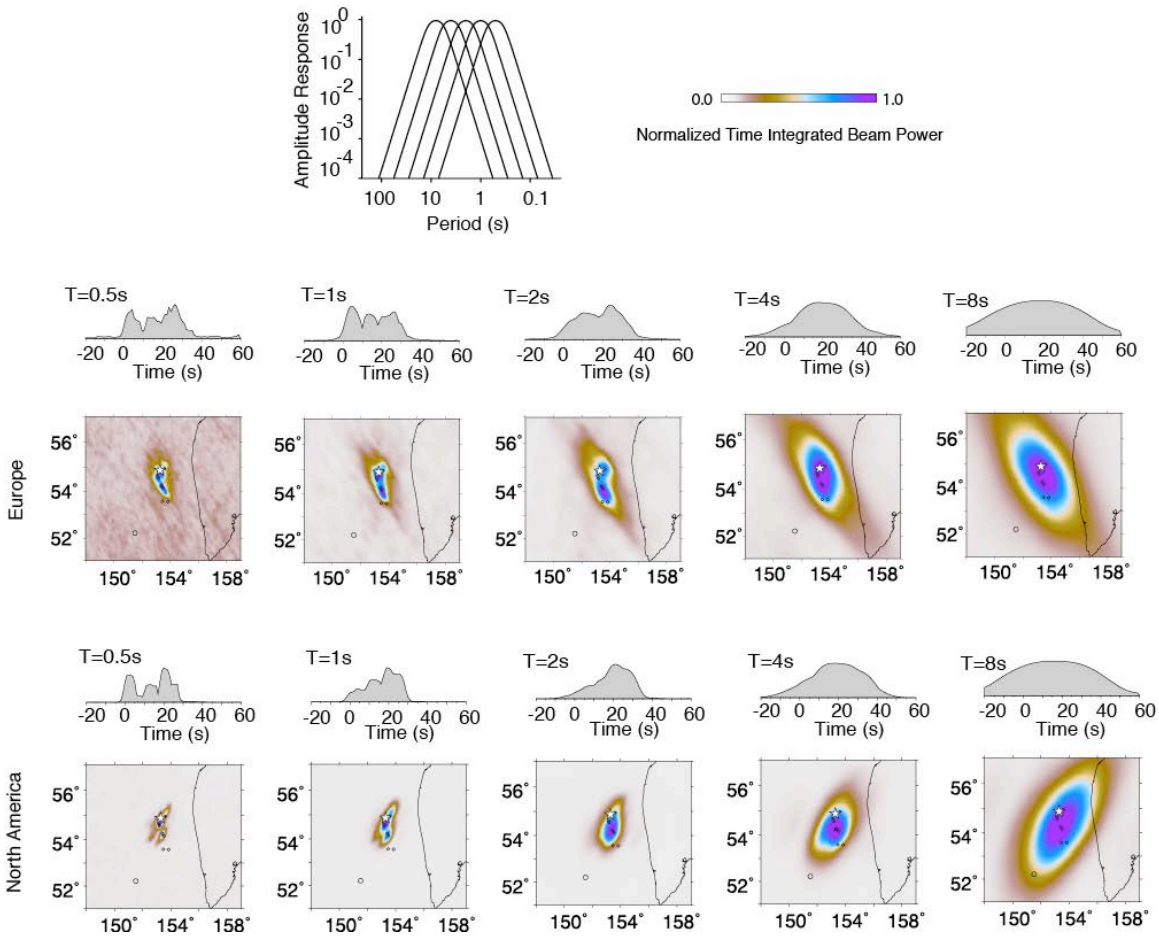

Fig. S8. Time-integrations of back-projections for a suite of narrow-band filtered P waves. The results for Europe and North American observations are shown. The narrowband filters are shown at the top left. The time-integrated back-projection for the P waves in each passband, aligned by the broadband signal correlations, are shown in the maps, with time-variation of peak image amplitude shown above each image. The decreasing temporal and spatial resolution with increasing period is a consequence of reduction of the move-out time lags for the finite-rupture relative to the dominant period of the signals.

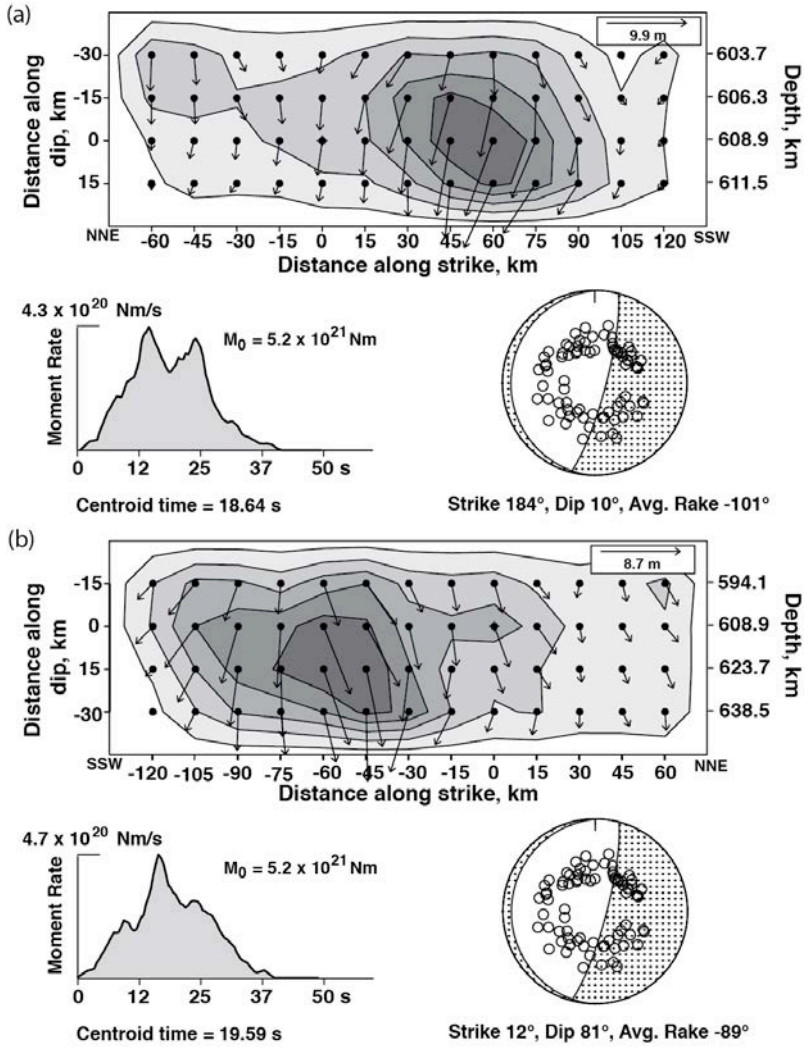

Fig. S9. The preferred rupture models. These models are for (a) the shallow dipping fault plane and (b) the steeply dipping fault plane. Both have a rupture velocity of 4.0 km/s, with the along-strike dimension being compatible with the back-projection images in Fig. S4, and the along-dip dimension being constrained so that the calculated stress drop for the average slip for subfaults with moment at least 15-20% of the largest subfault moment is 15 MPa, using the formula for a contained dip-slip fault with a width of 60 km. For this stress drop, the radiation efficiency is compatible with a Mode III crack with corresponding rupture velocity (Fig. 4). The upper figure in each part shows the slip model with vectors indicating the variable rake on the fault (motion of the upper block relative to the lower block) with slip contoured in m. The source moment rate function is shown at the lower left, and has a centroid time of 18.6 s, compatible with the W-phase inversion centroid time. The focal mechanism shows the faulting geometry and gives the average rake of the fault model (strike and dip are fixed), and the take-off angles of P waves used in each inversion are shown. The corresponding waveform matches for the model in (a) are in Fig. S10.

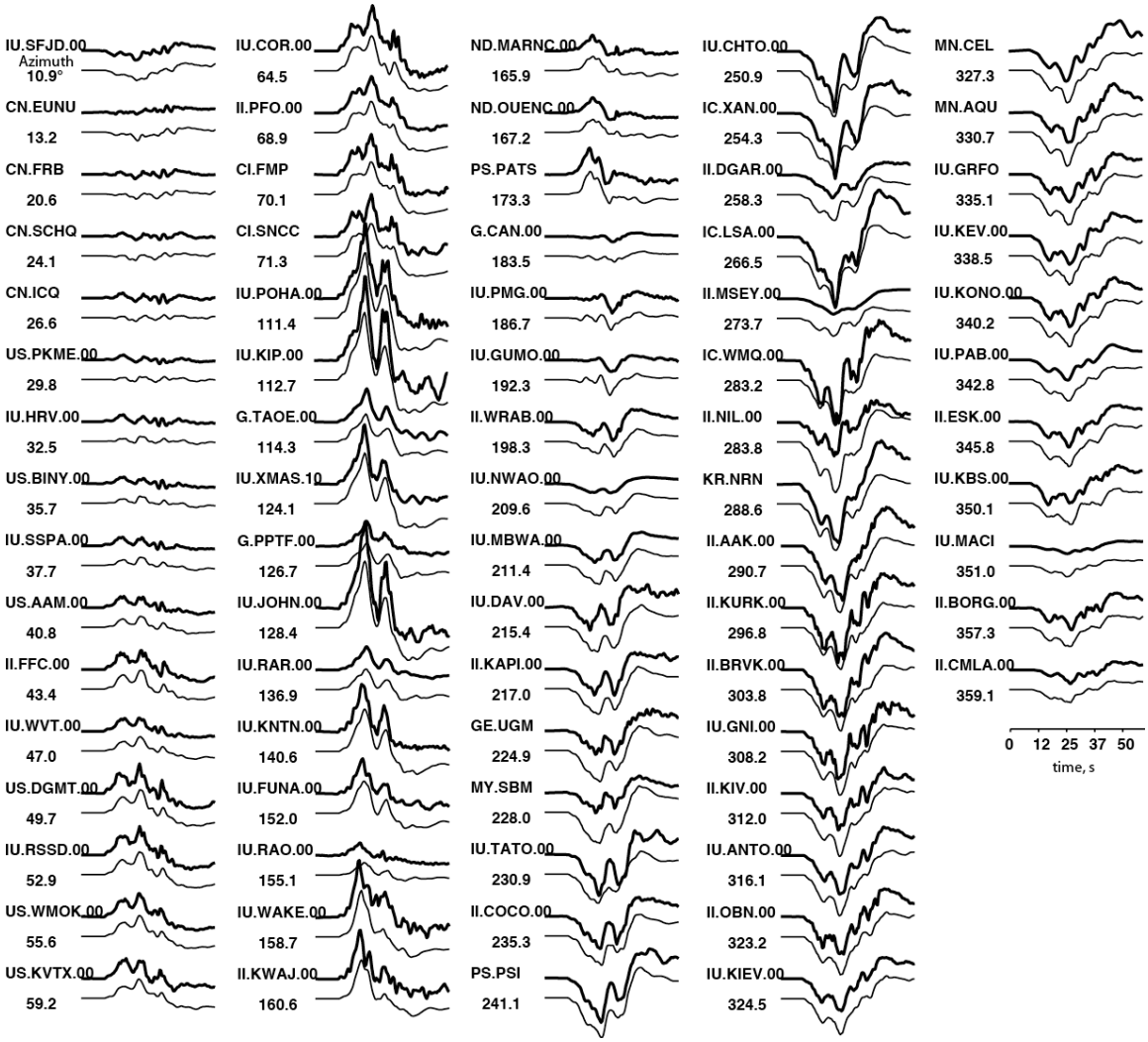

Fig. S10. P wave observations and predictions for the preferred shallow dipping model. Comparison of global teleseismic P wave observations (bold lines) and synthetics (light lines) for all data used in the finite-fault inversion in Fig.1 and Fig. S9a. Each station name and azimuth is given and all amplitudes are on a common scale. A 60 s time window with 10 s leader was used in the inversion.

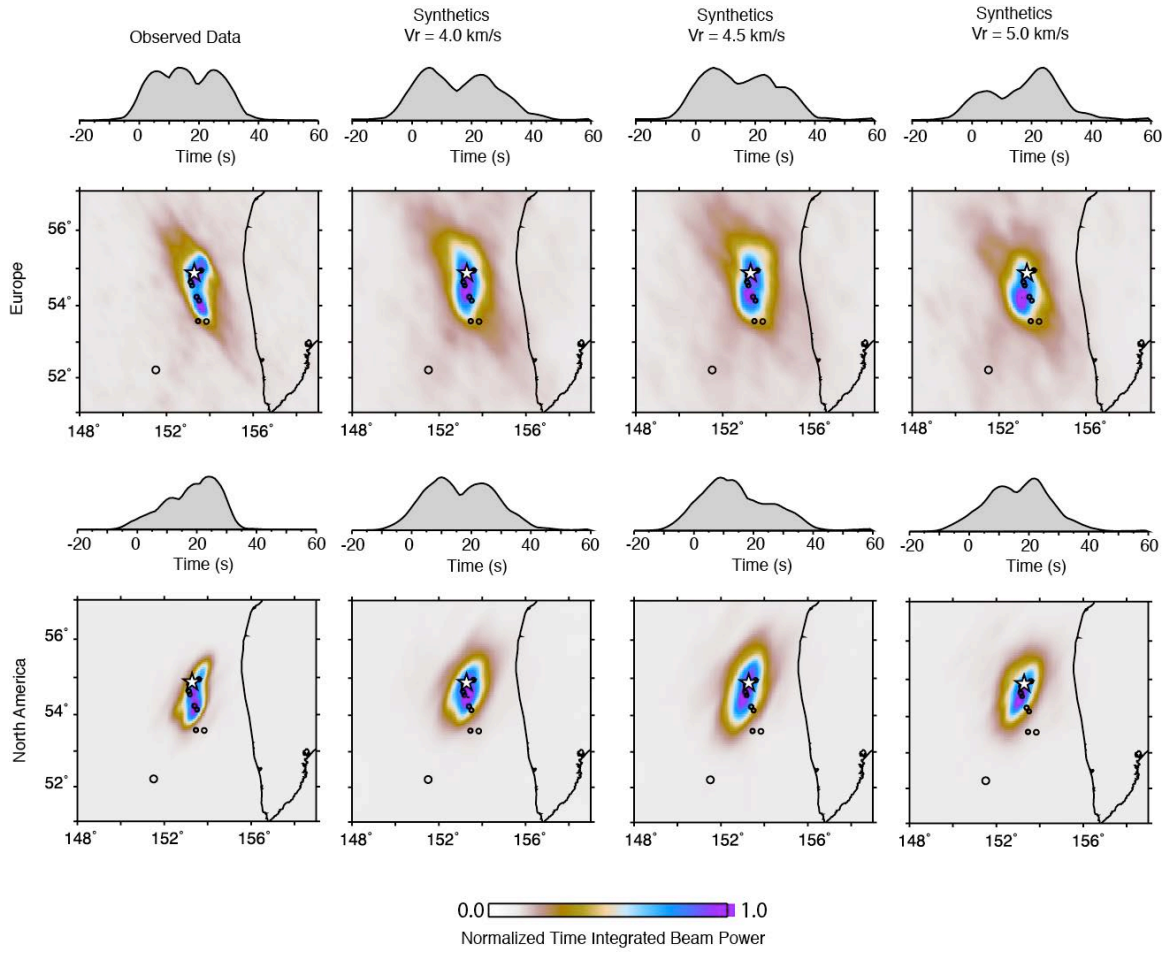

Fig. S11. Comparison of observed and synthetic back-projections. The time-integrated maps for back-projections of the data from Europe and North America (left column) are compared with back-projections for rupture models with varying rupture velocity that satisfy the radiation efficiency as shown in Fig. 4. The synthetics were made at the same stations and processed the same way as the data. The period range is 0.5-2.0 s. Models for the shallow-dipping fault plane (as in Fig. S9a) are shown Very similar comparisons are found for synthetics for models with the steeply dipping fault plane (as in Fig. S9b), with somewhat narrower features being imaged.

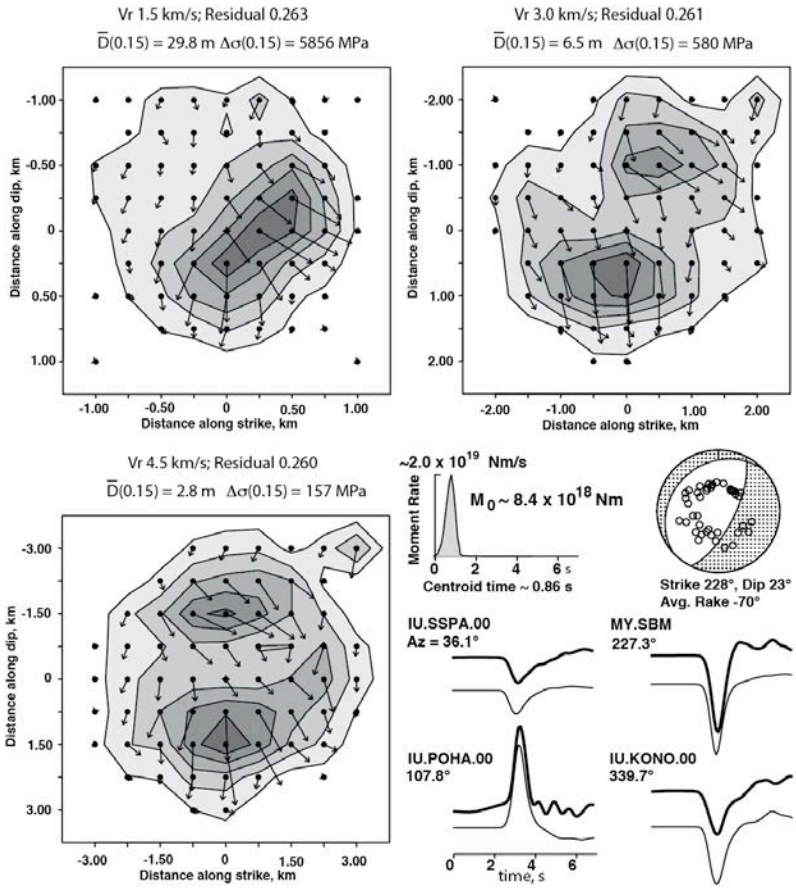

Fig. S12. Aftershock finite-fault models for varying rupture velocity. Slip distributions for three models with different constant rupture velocity with grid spacing scaling proportional to grid velocity. The strike is 228° and dip is 23° for all cases. Compact model grids are used, with the hypocenter located at the center of each grid. For small *Vr* the rupture is relatively circular, but as it increases the slip pattern develops two small patches. There is negligible difference in fit to the data for the different rupture models. For each model, the average displacement is computed for only those subfault sources with a seismic moment at least 15% as large as the largest sub-fault seismic moment and these values are given as D(0.15). Using the corresponding area of the remaining subfaults, a static stress drop is calculated using a circular rupture with radius matching the area of significant slip. There is about a factor of 37 range in stress drop estimate, and the stress drop is in the range 157 MPa to 5856 MPa. All of the inversions give similar source time functions, seismic moments and centroid times, with representative values being shown along with the average focal mechanism. Examples of waveform data (bold lines) and synthetics (thin lines) are shown, indicating the very short pulse of the teleseismic P wave signal, with some stations having minor broadening due to attenuation or slab diffraction. The energetic, short-duration impulse nature of the source made it a good empirical Green function event.

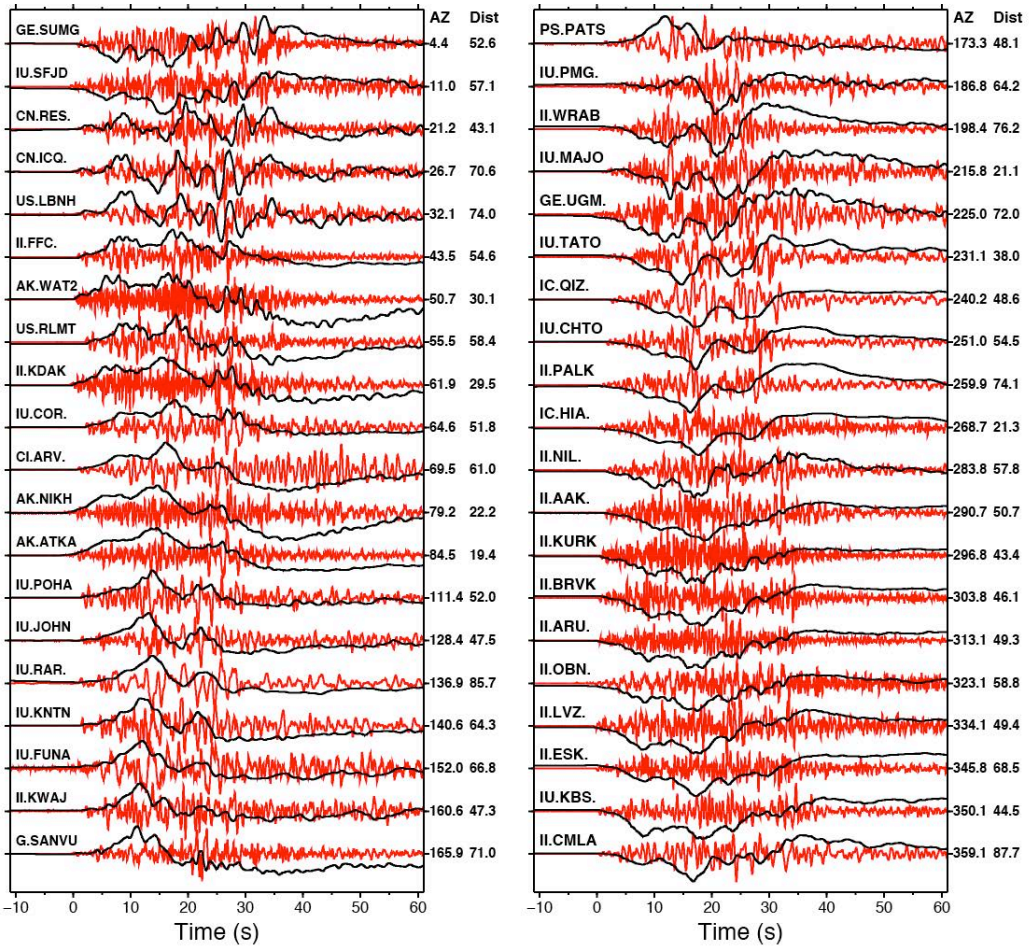

Fig. S13. Ground motion accelerations and displacements. Teleseismic P wave recordings from globally distributed broadband seismic stations for the 2013 Sea of Okhotsk event are shown, with the ground displacements given by the black lines and the corresponding ground accelerations given by the red lines. There is good correspondence between the overall temporal distribution of ground accelerations and the displacements (both are free of interference with surface reflections), and this supports use of short-period back-projection as a guide on the rupture kinematics.

Movie S1. Animation of back-projections of 0.5-2.0 Hz P waves for North America (NA) and European (EU) stations for the 2013 Okhotsk mainshock. The short-period P wave beam power stacked on a horizontal grid of possible source locations is shown as a function of time for the NA (left) and EU (right) stations distributions shown in Fig. S4. The color scale ranges from zero beam power (white) to unity normalized beam power (purple). The peak beam power at each time increment is tracked at the top with the sliding red bar indicating the time. This produces an approximation of the short-period energy radiation time history toward each network.

Supplementary References

S1. H. Hartzell, T. H., Heaton, *Bull. Seism. Soc. Amer.***73**, 1553 (1983)

S2. http://www.eri.u-tokyo.ac.jp/ETAL/KIKUCHI

S3. C. L. Lawson, R. J. Hanson, *Solving Least Squares Problems*, Society for Industrial Mathematics. (1995)

S4. Y. Xu, K. D. Koper, O. Sufri, L. Zhu, A. R, Hutko, *Geochem. Geophys. Geosyst*. **10**, Q04006 (2009).

S5. J. C. VanDecar, R. Crosson, *Bull. Seismol. Soc. Am*. **80**, 150 (1990).

S6. M. Schimmel, H. Paulssen, *Geophys. J. Int.* **130**, 497 (1997).

References and Notes

1. H. W. Green II, H. Houston, The mechanics of deep earthquakes. *Annu. Rev. Earth Planet. Sci.* **23**, 169–213 (1995). doi:10.1146/annurev.ea.23.050195.001125

2. H. W. Green II, P. C. Burnley, A new self-organizing mechanism for deep-focus earthquakes. *Nature* **341**, 733–737 (1989). doi:10.1038/341733a0

3. H. Kanamori, D. L. Anderson, T. H. Heaton, Frictional melting during the rupture of the 1994 Bolivian earthquake. *Science* **279**, 839–842 (1998). Medline doi:10.1126/science.279.5352.839

4. U.S. Geological Survey, http://earthquake.usgs.gov/earthquakes/eventpage/usb000h4jh#summary.

5. Global Centroid Moment Tensor Project, www.globalcmt.org/CMTsearch.html.

6. P. G. Silver, S. L. Beck, T. C. Wallace, C. Meade, S. C. Myers, D. E. James, R. Kuehnel, Rupture characteristics of the deep Bolivian earthquake of 9 June 1994 and the mechanism of deep-focus earthquakes. *Science* **268**, 69–73 (1995). doi:10.1126/science.268.5207.69

7. M. Kikuchi, H. Kanamori, The mechanism of the Deep Bolivia Earthquake of June 9, 1994. *Geophys. Res. Lett.* **21**, 2341–2344 (1994). doi:10.1029/94GL02483

8. S. L. Beck, P. Silver, T. C. Wallace, D. James, Directivity analysis of the Deep Bolivian Earthquake of June 9, 1994. *Geophys. Res. Lett.* **22**, 2257–2260 (1995). doi:10.1029/95GL01089

9. P. F. Ihmlé, On the interpretation of subevents in teleseismic waveforms: The 1994 Bolivia deep earthquake revisited. *J. Geophys. Res.* **103**, 17,919 (1998). doi:10.1029/98JB00603

10. W.-P. Chen, *En echelon* ruptures during the Great Bolivian Earthquake of 1994. *Geophys. Res. Lett.* **22**, 2261–2264 (1995). doi:10.1029/95GL01805

11. M. Antolik, D. Dreger, B. Romanowicz, Finite fault source study of the Great 1994 Deep Bolivia Earthquake. *Geophys. Res. Lett.* **23**, 1589–1592 (1996). doi:10.1029/96GL00968

12. D. A. Wiens, J. J. McGuire, The 1994 Bolivia and Tonga events: Fundamentally different types of deep earthquakes? *Geophys. Res. Lett.* **22**, 2245–2248 (1995). doi:10.1029/95GL01598

13. A. Venkataraman, H. Kanamori, Observational constraints on the fracture energy of subduction zone earthquakes. *J. Geophys. Res.* **109**, B05302 (2004). doi:10.1029/2003JB002549

14. L. Rivera, H. Kanamori, Representations of the radiated energy in earthquakes. *Geophys. J. Int.* **162**, 148–155 (2005). doi:10.1111/j.1365-246X.2005.02648.x

15. H. Kanamori, L. Rivera, Energy partitioning during an earthquake. *AGU Geophys. Monogr.* **170**, 3–13 (2006). doi:10.1029/170GM03

16. A. V. Newman, E. A. Okal, Teleseismic estimates of radiated seismic energy: The E/M_0 discriminant for tsunami earthquakes. *J. Geophys. Res.* **103**, 26885 (1998). doi:10.1029/98JB02236

17. N. W. Winslow, L. J. Ruff, A hybrid method for calculating the radiated wave energy of deep earthquakes. *Phys. Earth Planet. Inter.* **115**, 181–190 (1999). doi:10.1016/S0031-9201(99)00077-1

18. H. Noda, N. Lapusta, H. Kanamori, Comparison of average stress drop measures for ruptures with heterogeneous stress change and implications for earthquake physics. *Geophys. J. Int.* **193**, 1691–1712 (2013). doi:10.1093/gji/ggt074

19. L. B. Freund, Energy flux into the tip of an extending crack in an elastic solid. *J. Elast.* **2**, 341–349 (1972). doi:10.1007/BF00045718

20. A. F. Fossum, L. B. Freund, Nonuniformly moving shear crack model of a shallow focus earthquake mechanism. *J. Geophys. Res.* **80**, 3343–3347 (1975). doi:10.1029/JB080i023p03343

21. B. V. Kostrov, Unsteady propagation of longitudinal shear cracks. *J. Appl. Math. Mech. Engl. Transl* **30**, 1241–1248 (1966). doi:10.1016/0021-8928(66)90087-6

22. N. F. Mott, *Engineering* **165**, 16 (1948).

23. H. Kanamori, E. Brodsky, The physics of earthquakes. *Rep. Prog. Phys.* **67**, 1429–1496 (2004). doi:10.1088/0034-4885/67/8/R03

24. B. P. Allmann, P. M. Shearer, Global variations of stress drop for moderate to large earthquakes. *J. Geophys. Res.* **114**, B01310 (2009). doi:10.1029/2008JB005821

25. J. A. Convers, A. V. Newman, Global evaluation of large earthquake energy from 1997 through mid-2010. *J. Geophys. Res.* **116**, B08304 (2011). doi:10.1029/2010JB007928

26. T. Lay, H. Kanamori, C. J. Ammon, A. R. Hutko, K. Furlong, L. Rivera, The 2006–2007 Kuril Islands great earthquake sequence. *J. Geophys. Res.* **114**, B11308 (2009). doi:10.1029/2008JB006280

27. H. Houston, H. M. Benz, J. E. Vidale, Time functions of deep earthquakes from broadband and short-period stacks. *J. Geophys. Res.* **103**, 29895 (1998). doi:10.1029/98JB02135

28. W.-Y. Chung, H. Kanamori, Variation of seismic source parameters and stress drops within a descending slab and its implications in plate mechanics. *Phys. Earth Planet. Inter.* **23**, 134–159 (1980). doi:10.1016/0031-9201(80)90008-4

29. L.-R. Wu, W.-P. Chen, Rupture of the large (M_w 7.8), deep earthquake of 1973 beneath the Japan Sea with implications for seismogenesis. *Bull. Seismol. Soc. Am.* **91**, 102–111 (2001). doi:10.1785/0120000081

30. R. Tibi, G. Bock, D. A. Wiens, Source characteristics of large deep earthquakes: Constraint on the faulting mechanism at great depths. *J. Geophys. Res.* **108**, 2091 (2003).